Science Advances
AAAS

advances.sciencemag.org/cgi/content/full/6/50/eabd1919/DC1

Supplementary Materials for

Ultrahigh-resolution scanning microwave impedance microscopy of moiré lattices and superstructures

Kyunghoon Lee, M. Iqbal Bakti Utama, Salman Kahn, Appalakondaiah Samudrala, Nicolas Leconte, Birui Yang, Shuopei Wang, Kenji Watanabe, Takashi Taniguchi, M. Virginia P. Altoé, Guangyu Zhang, Alexander Weber-Bargioni, Michael Crommie, Paul D. Ashby, Jeil Jung, Feng Wang*, Alex Zettl*

*Corresponding author. Email: azettl@berkeley.edu (A.Z.); fengwang76@berkeley.edu (F.W.)

Published 9 December 2020, *Sci. Adv.* **6**, eabd1919 (2020)
DOI: 10.1126/sciadv.abd1919

This PDF file includes:

Figs. S1 to S16

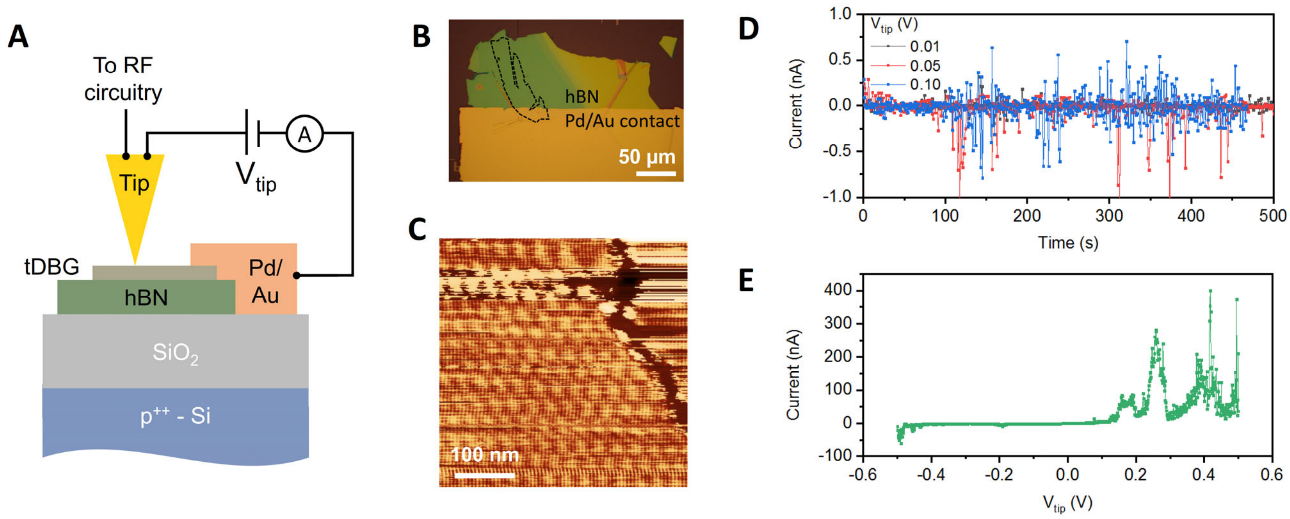

Fig. S1. Tip-sample leak current. We characterized the type of electrical coupling between the uMIM tip (made of Au and TiW) and a tDBG device as the tip is scanning the moiré lattice in contact mode. **(A)** The schematic of the measurement. An electrical contact to the tDBG (Pd/Au film) was made by e-beam evaporation through a shadow mask to ensure surface cleanliness. The application of DC tip bias (V_{tip}) and current measurement were done via an external sourcemeter. **(B)** Optical micrograph of the sample. The area with graphene (including tDBG) is marked with the black dashed line. **(C)** An example of the moiré lattice imaged while a constant $V_{tip} = 0.05$ V is applied. **(D)** As the moiré lattice is imaged, a finite constant V_{tip} is applied and the current passing in the circuit shown in (A), is monitored. For $|V_{tip}| \leq 0.1$V, the measured current is only within the noise level (~0.1 nA). Thus, the resistance between the tip and sample is larger than 1 GΩ. **(E)** The measured current as the V_{tip} is swept between -0.5–0.5 V. Appreciable leak current starts to show at larger V_{tip} as the resistance drops to ~1 MΩ. Given that the moiré lattice can be imaged regardless of the electrical contact resistance between the tip and the sample, these measurements indicate that an Ohmic contact between the tip and sample is not required to achieve the ultra-high-resolution moiré imaging. The possibility to image the moiré with highly resistive contact (fig. S1E) also suggests that the high resolution we achieved cannot be explained by a current-assisted signal enhancement mechanism.

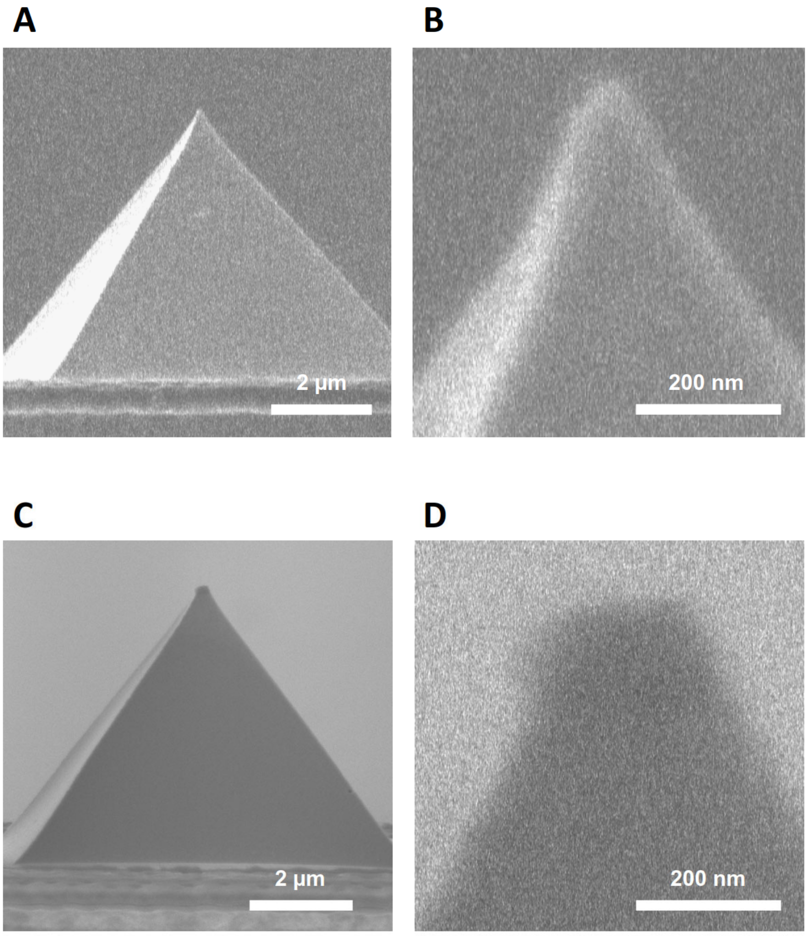

Fig. S2. SEM images of new and used uMIM tips. Low and high magnification images are shown for each tip. **(A-B),** SEM images of a new, unused tip similar to that shown in Fig. 1A in the main text. **(C-D)** SEM images of a tip that has been used to perfom ultra-high-resolution contact mode uMIM imaging of the moiré lattice in tDBG samples. At this scale, apparent significant degradation of the tip sharpness is observed in the used tip. However, the used tip remains capable of providing high resolution imaging and resolves the moiré pattern. Our result is consistent with a previous report where tip blunting does not necessarily degrade the sMIM resolving power in contact mode (*32*).

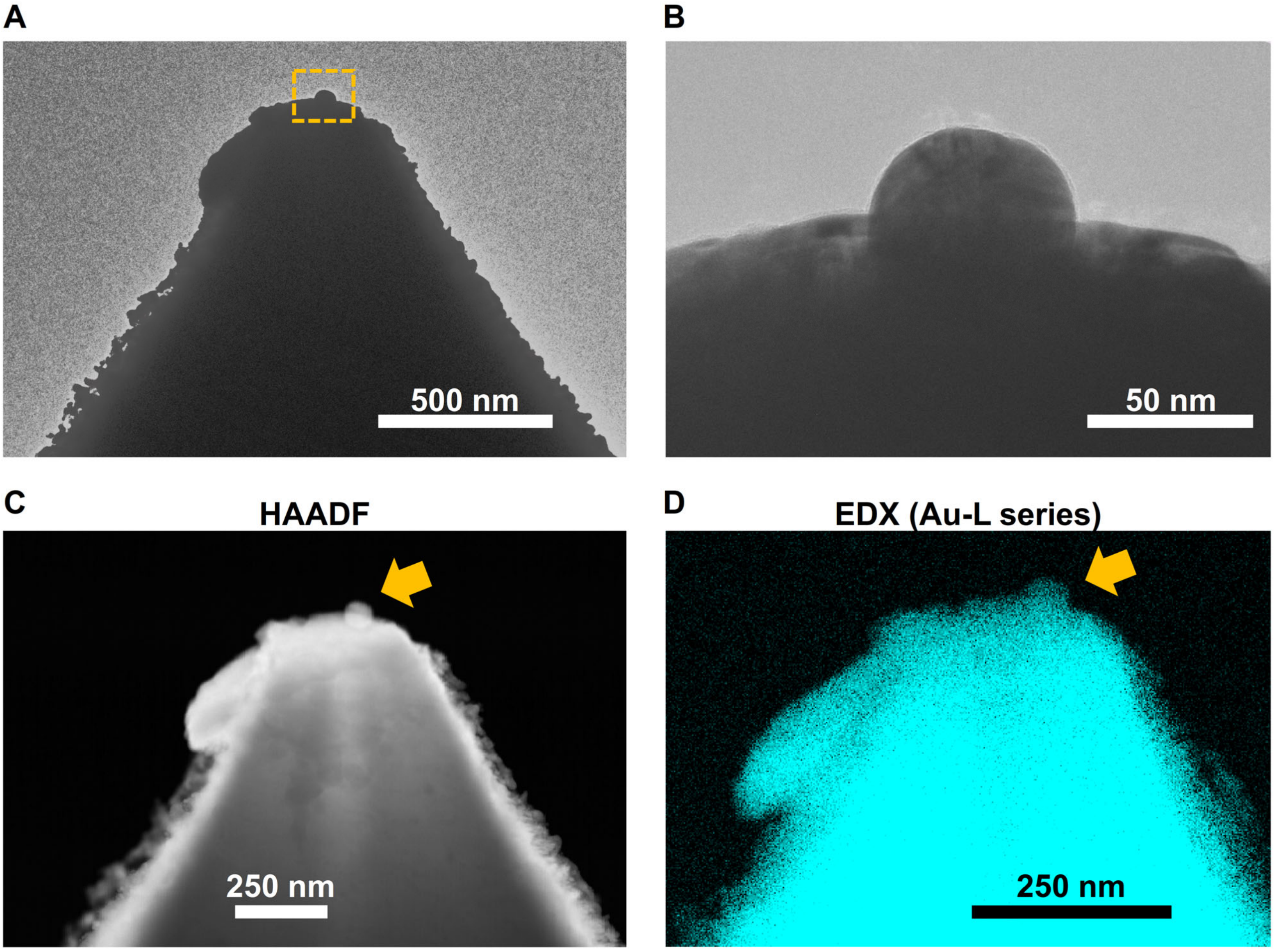

Fig. S3. TEM images of a used uMIM tip. (A) Bright field TEM image of the tip. **(B)** Zoomed-in bright field image on the area indicated by dashed orange square in (A). At a gross length scale (as for fig. S2D), the used tip will have an apparent apex geometry that is blunter than that of an unused tip (*e.g.*, fig. S2). However, we have observed that the used tip may deform to create a metallic protrusion at the apex that causes the effective tip radius to be smaller than the gross tip radius. **(C)** STEM image using high angle annular dark field (HAADF) detector. Since the HAADF mode is a Z-contrast imaging, the strong signal from the protrusion at the apex suggests that it is indeed metallic. **(D)** Spatial map of the energy dispersive x-ray (EDX) spectrum from the Au L-series. The map shows that the protrusion contains Au signal, similar to the rest of the tip body, suggesting that the protrusion primarily comes from the tip deformation after scanning.

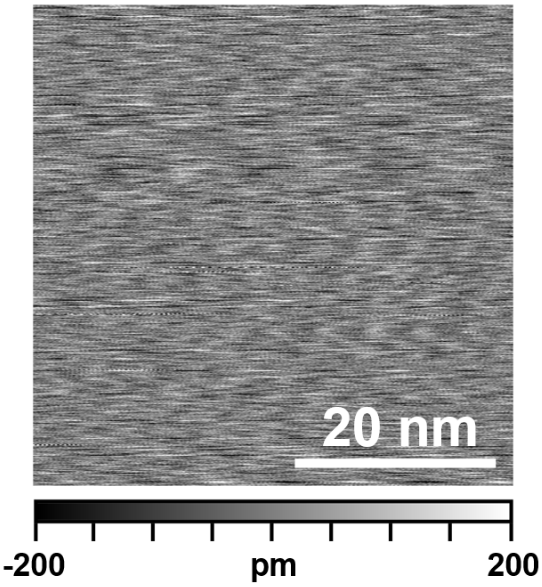

Fig. S4. Topography image of the magic-angle tDBG. Unlike in the maps of the uMIM signal as shown in Fig. 1D and E of the main text, the topography channel does not reveal the triangular lattice feature that corresponds to the moiré lattice. This result strengthens the attribution of the uMIM signal modulation to the moiré lattice, rather than purely from topographic artifact.

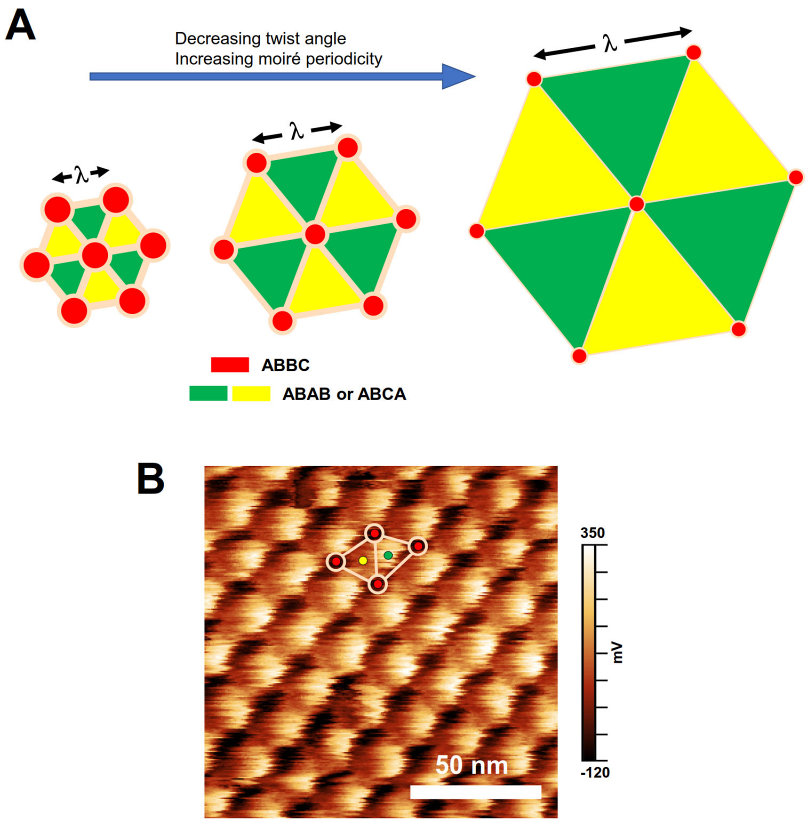

Fig. S5. Assignment of the ABBC domains in tDBG. (A) A schematic illustration of the relative sizes of the domains to the moiré unit cell as a function of the twist angle. *(Left)* At large twist angle, the circular ABBC domains occupy an appreciable proportion of the moiré unit cell. This situation is represented by the moiré lattice in Fig. 1d of the main text, which has a twist angle of 1.3°. *(Middle)* as the twist angle is reduced to less than ~1°, lattice relaxation start to occur. The relaxation causes the triangular ABAB and ABCA region to grow larger in proportion to the moiré unit cell size, shrinking the relative size of the ABBC domain. *(Right)* As the twist angle approaches 0°, the ABBC domains become much smaller and the moiré lattice is now dominated by the ABAB and ABCA domains of relatively similar sizes. This scenario is represented by Fig. 2C in the main text. **(B)** A uMIM-Im image of a tDBG at an area with a twist angle of (0.61 ± 0.04)°, corresponding to a moiré period of (23.1 ± 1.4) nm. Similar to Fig. 1D in the main text, the moiré lattice is also composed of three domains with distinct uMIM-Im signal. However, the domain with the weakest uMIM-Im signal has became noticeably smaller than the other two domains, which in turn have similar triangular shape and size. The situation in fig. S5B thus corresponds to the scheme in fig. S5A (*Middle*), and we can therefore identify the domain with the weakest uMIM-Im signal to the ABBC stacking. The illustration of the different domains in the moiré is superimposed on the image in (B).

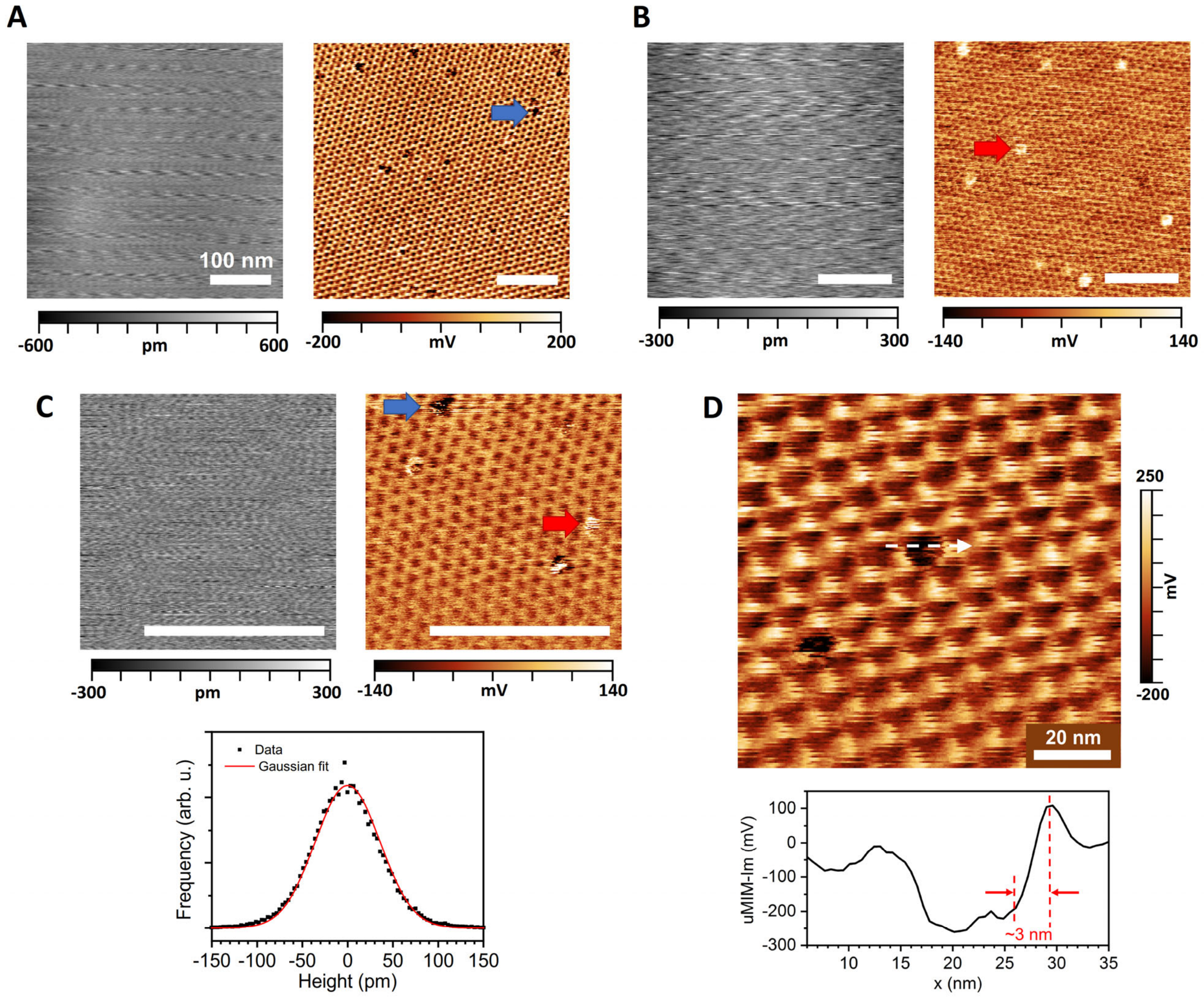

Fig. S6. Defects in moiré lattice of tDBG as observed in uMIM. The topography and the uMIM-Im images are shown. All scale bars correspond to 100 nm. Such defects in the moiré lattice appear analogous to the point defects in atomic lattice. **(A)** Moiré defects appearing as dark spots, implying a lower local conductivity than the surrounding moiré lattice. An example is marked by blue arrow. **(B)** Moiré defects appearing as bright spots, which has a higher conductivity than other domains in the moiré lattice. An example is marked by red arrow. **(C)** Bright and dark moiré defects appearing within the same uMIM-Im frame (red and blue arrows, respectively). The height histogram is also shown and fitted with a Gaussian distribution, giving σ = (36±1) pm. **(D)** An uMIM-Im image of an area near a dark moiré defect. The signal profile along the white dashed arrow is also shown. Consistent to the result in Fig. 1F-G in the main text, the capability to resolve the sub-5 nm isolated moiré defects unambiguously substantiate our imaging resolution. This is indicated by the ~3 nm "knife-edge" broadening of the uMIM signal at the edge of the moiré defect. Throughout fig. S6A-C the topography images do not exhibit any recognizable feature at the position of the moiré defects, and thus we can rule out topographic artefact (*e.g.*, large dust particles) as the origin of the defect signal in uMIM.

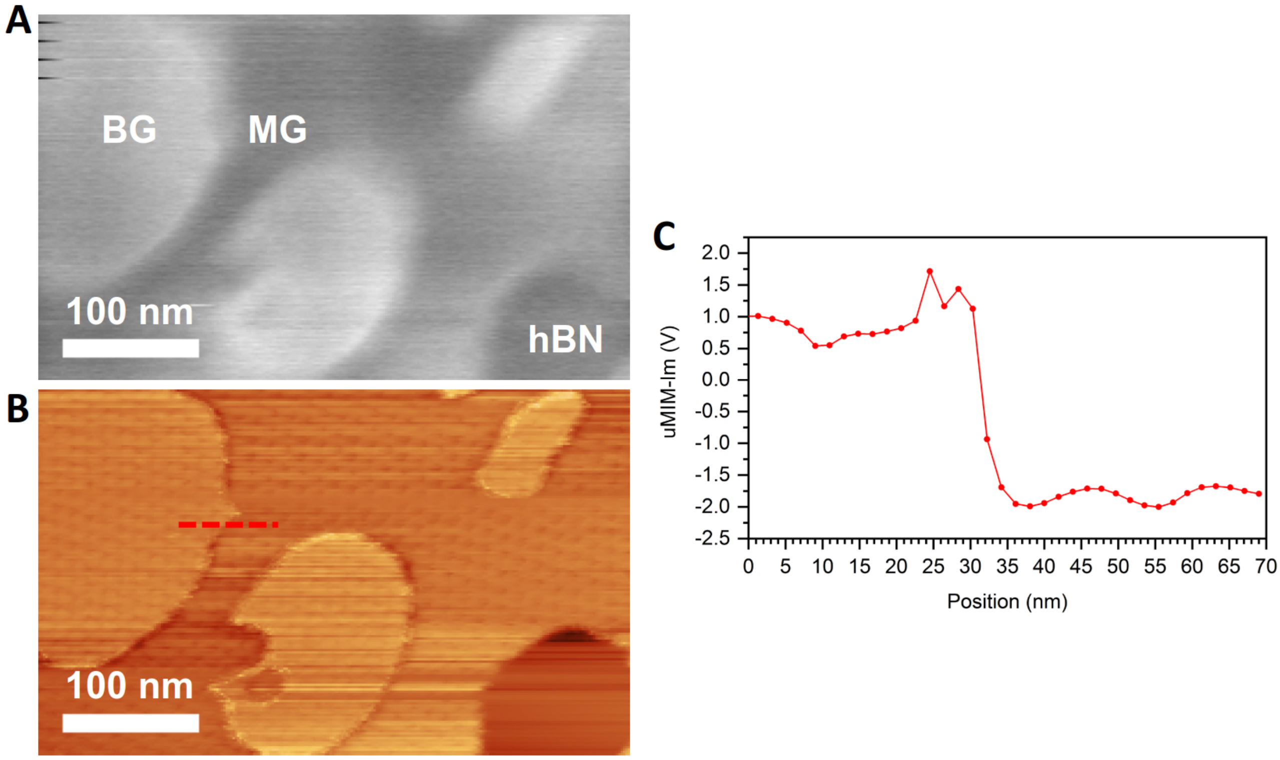

Fig. S7. Imaging around the borders of mono- and bilayer CVD graphene islands on hBN. (A) The topography image. The different regions of the sample are labelled (BG: bilayer graphene, MG: monolayer graphene). **(B)** uMIM-Im image of the same area as in (A). **(C)** The signal profile along the red dashed line in (B). The signals originating from bilayer and monolayer regions show sharp transition, demonstrating the sub-5 nm spatial resolution.

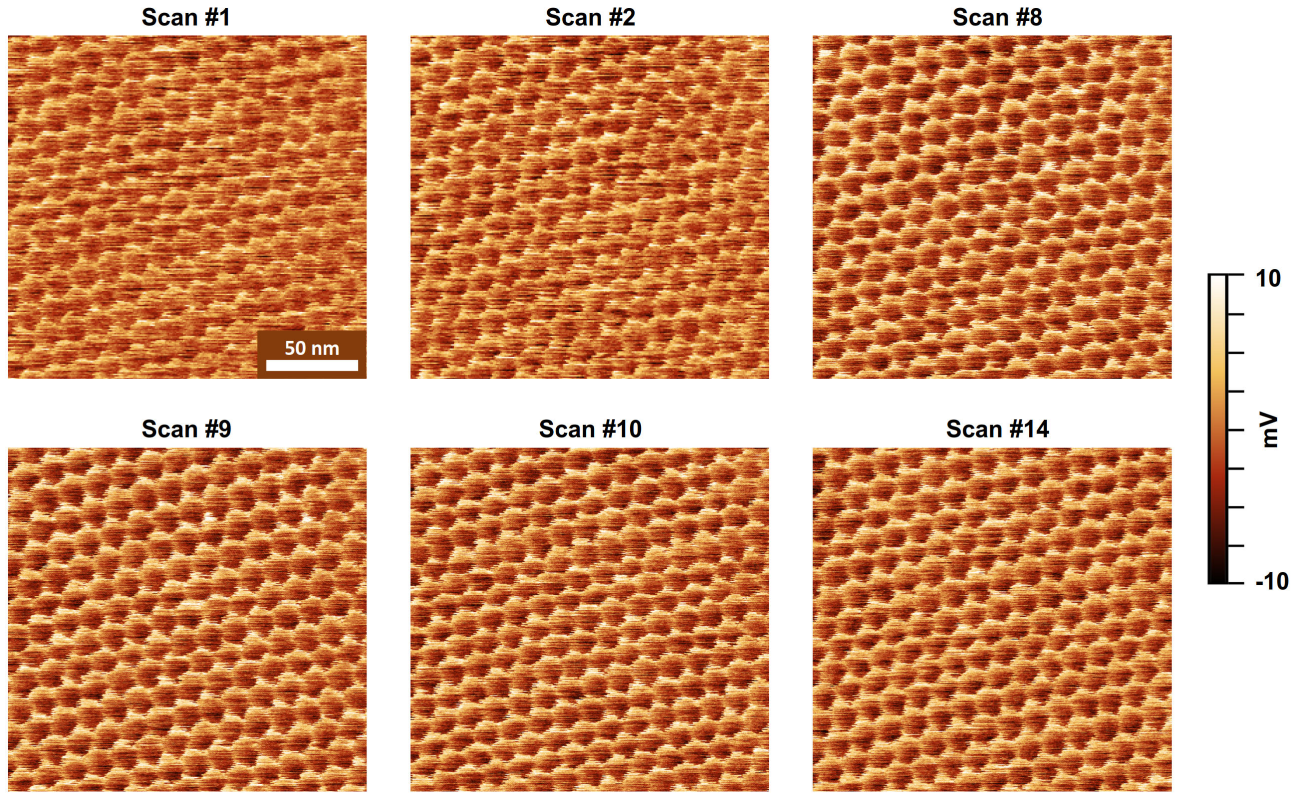

Fig. S8. Multiple uMIM scans of an epitaxial graphene/hBN. In our measurements, we have used a relatively low setpoint that corresponds to ~ 1-5 nN force between the tip and the sample. Similar level of force has been used for the contact mode AFM imaging of moiré lattice without report of sample damage from the probe (*e.g.*, 1 nN in Ref. (*22*)). As an evidence, we show here a series of uMIM-Im images of moiré lattice from graphene/hBN. Using the typical scanning condition, we scanned continuously within the same area of 200×200 nm^2 of the sample for more than 5 hrs. After many times of scanning (including trace and retrace), the moiré lattice is largely unchanged and no creation of irregular spots similar to the moiré defects were observed. This result suggests that the moiré defects may not originate simply from the probe tip induced damage.

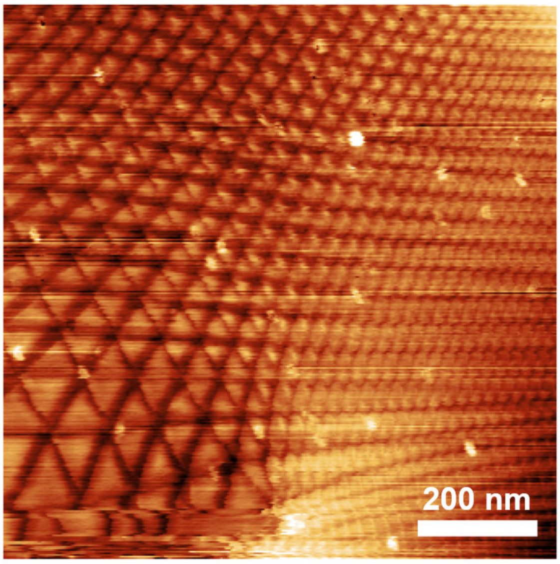

Fig. S9. Demonstration of uMIM in characterizing the inhomogeneity of the moiré lattice. The tDBG sample shown here exhibited an extreme example of spatial and structural inhomogeneity over a large area. The uMIM-Re map reveals an evolution of the lattice from the moiré pattern (right hand side) to a triangular network of domains and domain wall states (left hand side) within a tDBG sample. The evolution of the structure is a result of the local variation of the tDBG twist angle, such as due to strain.

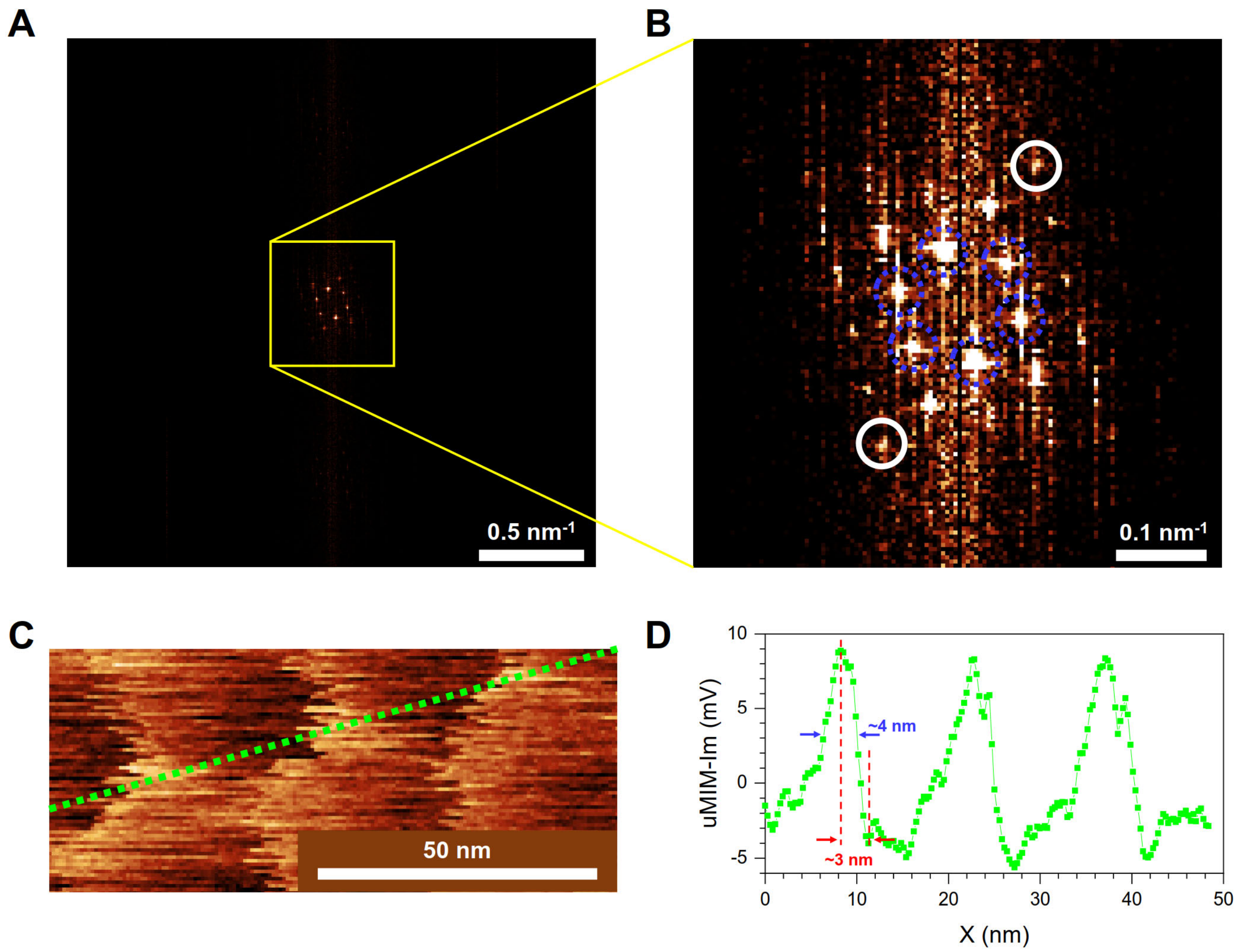

Fig. S10. Evaluating the spatial resolution of the epitaxial graphene/hBN image. (A) The full frame FFT from the real space uMIM-Im (from Fig. 2A upper row in the main text). The FFT shown as the inset in Fig. 2A in the main text was cropped from this figure. **(B)** The cropped area inside the yellow square in Fig. (A) but with an enhanced color contrast. The first-order spots that were used to determine the moiré period of graphene/hBN are marked with dotted blue circles. The white circles mark the highest order spots, which correspond to the smallest periodic feature that can be unambiguously registered. In real space, these spots correspond to a Fourier component with period of ~5.1 nm. The resulting image resolution should then be lower than this value. **(C)** A cropped uMIM-Im image from Fig. 2A lower row. **(D)** The line profile along the dotted green line in (C), where the line passes the vertices of the hexagonal domains. The profile shows that uMIM can resolve the moiré sub-unit cell features, with the FWHM of the spots at the vertices measured at ~4 nm and the signal saturating within ~3 nm.

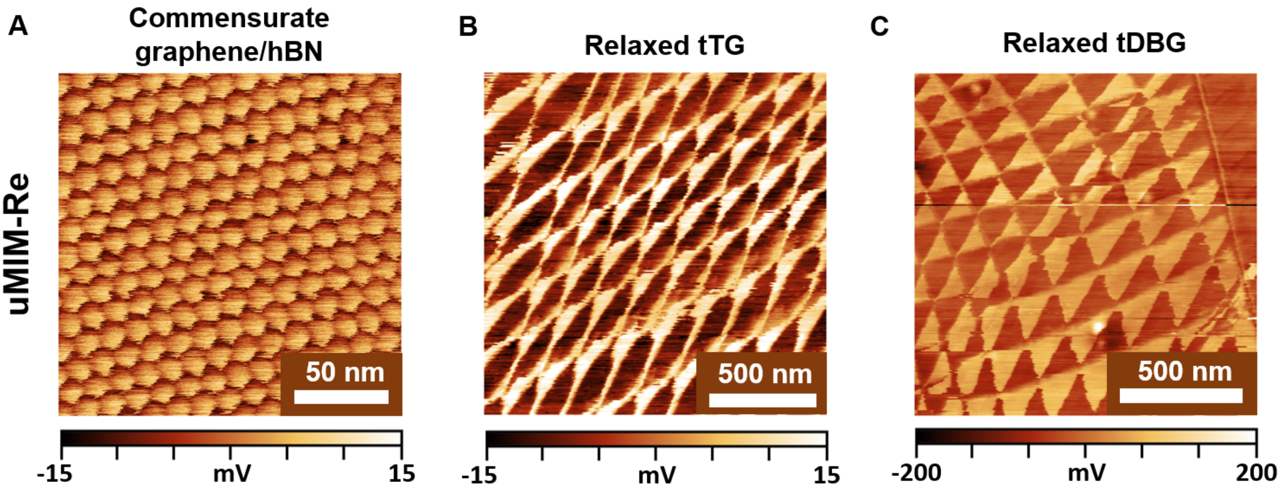

Fig. S11. The uMIM-Re images on various graphitic moiré lattices. (A) Commensurate, epitaxial monolayer graphene on hBN. **(B)** Relaxed tTG. **(C)** Relaxed tBG. These images correspond to the same sample location as the upper row images in Fig. 2 of the main text.

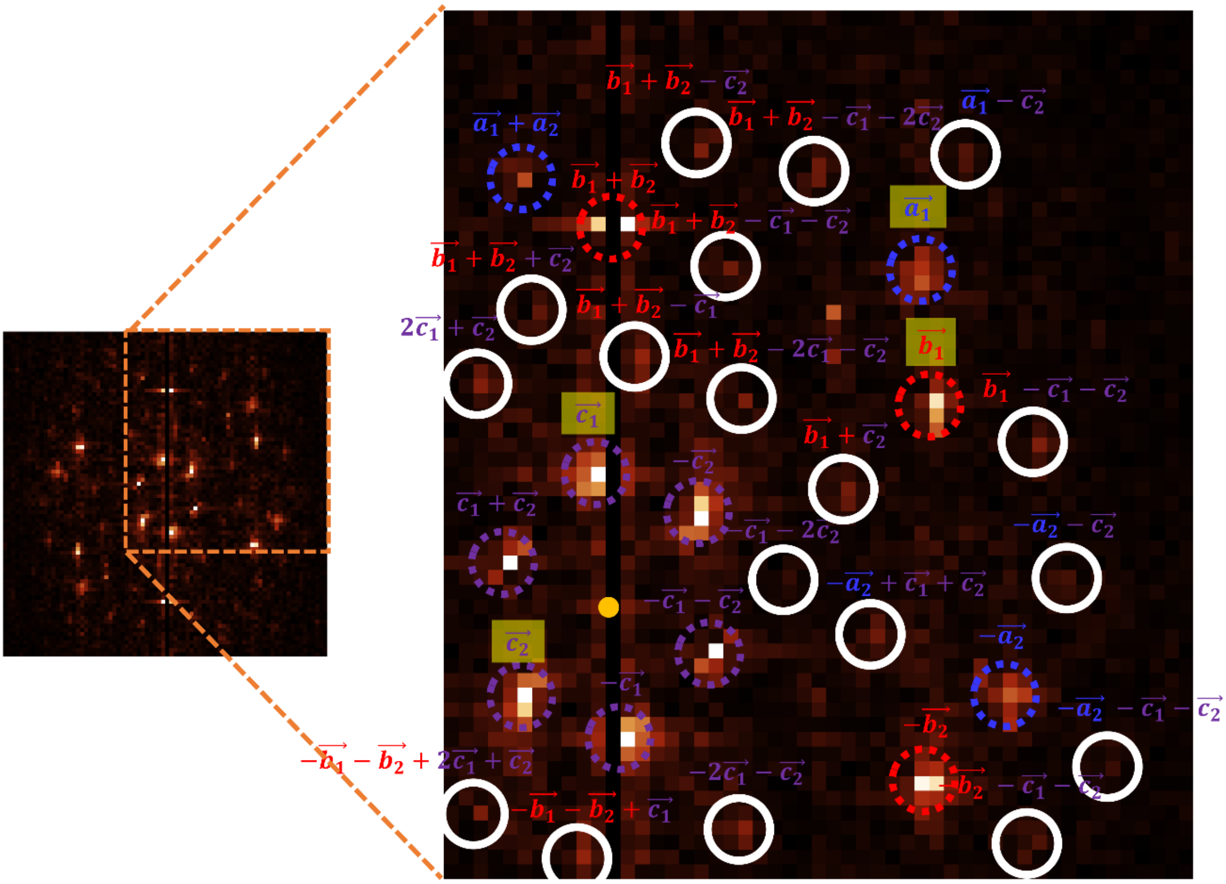

Fig. S12. The labelled FFT image of the moiré superlattice feature in tDBG/hBN sample. The region around the first-quadrant is shown while the spots for the remaining quadrants can be identified by inversion or rotation relative to the origin (orange circle). The spots circled with blue, red, and purple dotted borders are the first-order spots and the labels are shaded in yellow. The component of reciprocal vectors that defines the position of these spots are given as the label: $\vec{a_1}$ and $\vec{a_2}$ for BG/BG moiré (blue text), $\vec{b_1}$ and $\vec{b_2}$ for the BG/hBN moiré (red text), $\vec{c_1}$ and $\vec{c_2}$ for moiré superlattice (purple text), where $\vec{c_j} = \vec{a_j} - \vec{b_j}$.

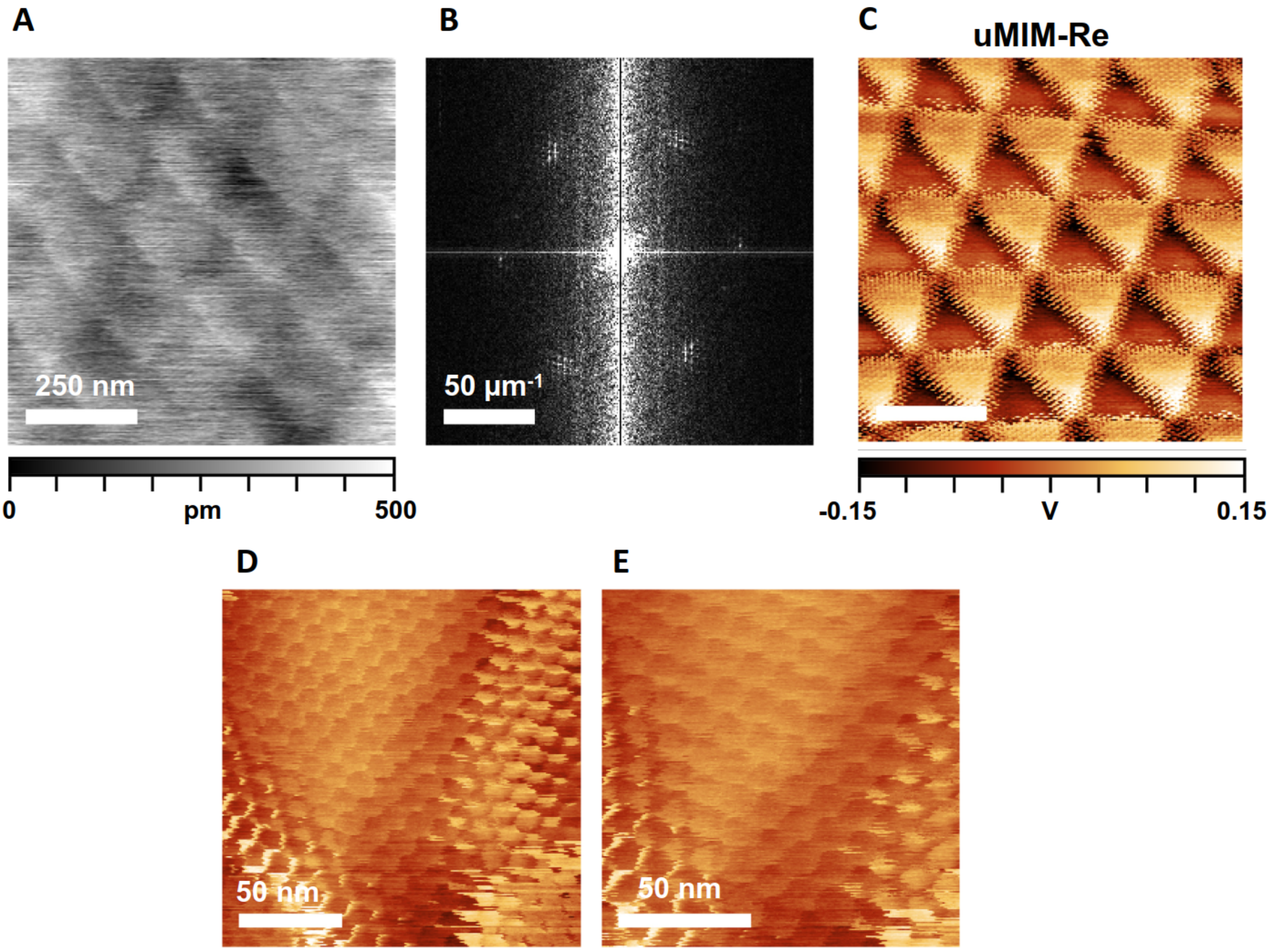

Fig. S13. Topography and uMIM-Re images of the composite between a relaxed tDBG lattice and a BG/hBN moiré. (A) Topography image. **(B)** The FFT of the topography image in (A). **(C)** uMIM-Re image of the same area. The figs. S13A-C were collected concurrently as the uMIM-Im image in the Fig. 3D of the main text. **(D-E)** Shrinking the scan area relative to that of the uMIM-Im image in Fig. 3G of the main text, showing the moiré pattern of BG/hBN inside the relaxed triangular domain and near the domain boundary.

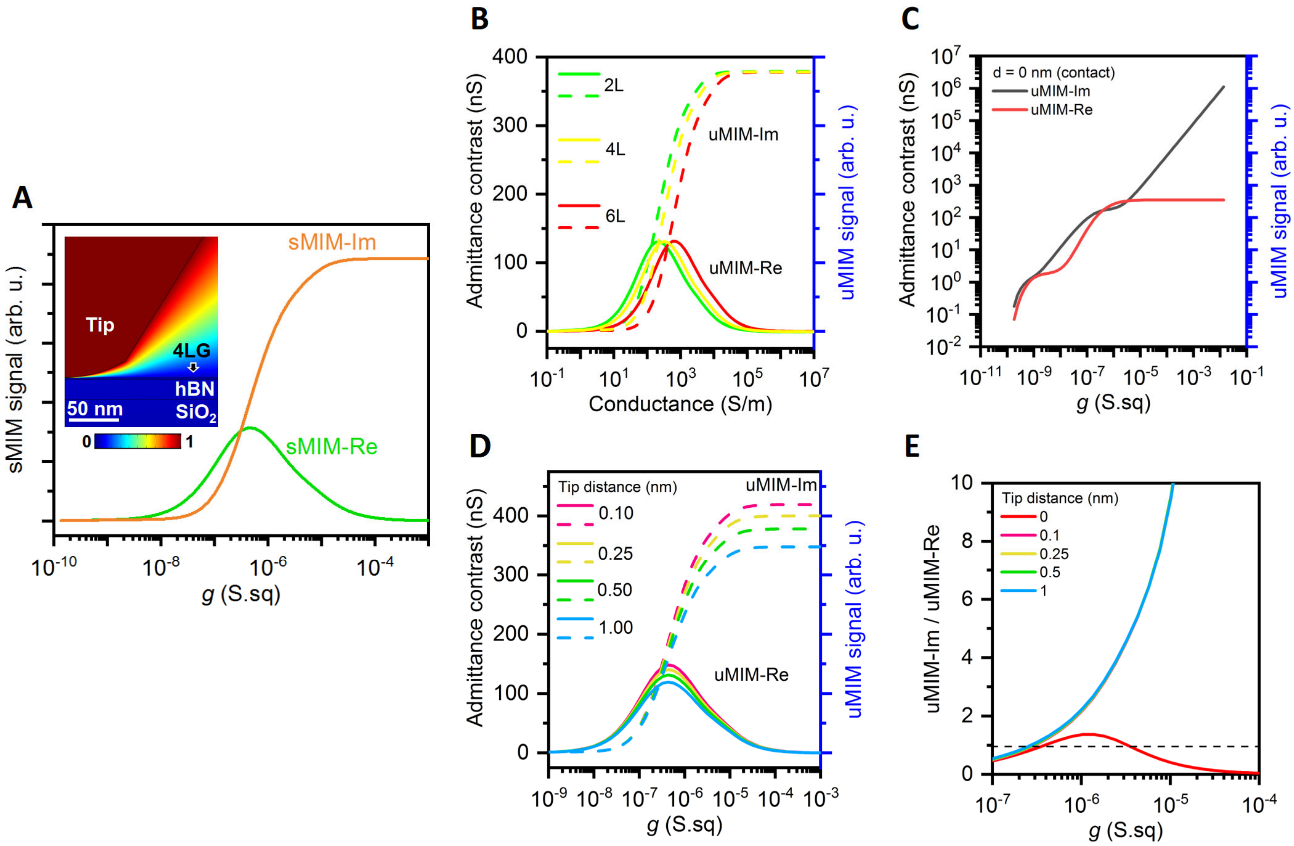

Fig. S14. Details in the finite element analysis. (A) Calculated sMIM signal based on the gross geometry of the tip as determined from SEM. *Inset*: Simulated quasi-static potential. **(B)** Dependence on the admittance contrast on the sample thickness. The sMIM response curves are only relatively shifted with increasing layer number of graphene. Thus, we have normalized these thickness dependences by plotting the simulation as a function of the 2D sheet conductance in Fig. 1B of the main text. **(c)** The admittance contrast, and thus the uMIM response curves with the assumption of contacting tip and sample (*i.e.*, zero tip-sample distance). Both the uMIM-Im and uMIM-Re signals are continuously increasing with increasing sample conductance. This simulation result is not compatible with our experimental observation, where the relative uMIM-Im and uMIM-Re between different local stacking in tDBG tend to have the opposite trend. This suggests that the experimental uMIM-Re signal strength has a negatively correlated trend with the sample conductance within the regime of the experimental condition. **(D)** The admittance contrast as a function of the tip-sample distance. Assumption of a finite tip-distance, resulting in capacitive coupling between tip and sample, agrees with the observation of non-ohmic contact as discussed in fig. S1. **(E)** The ratio of the real and imaginary parts of admittance contrast for different tip-sample distance. This result establishes that the ratio between the imaginary and real signals is only weakly dependent on the finite tip-sample distance.

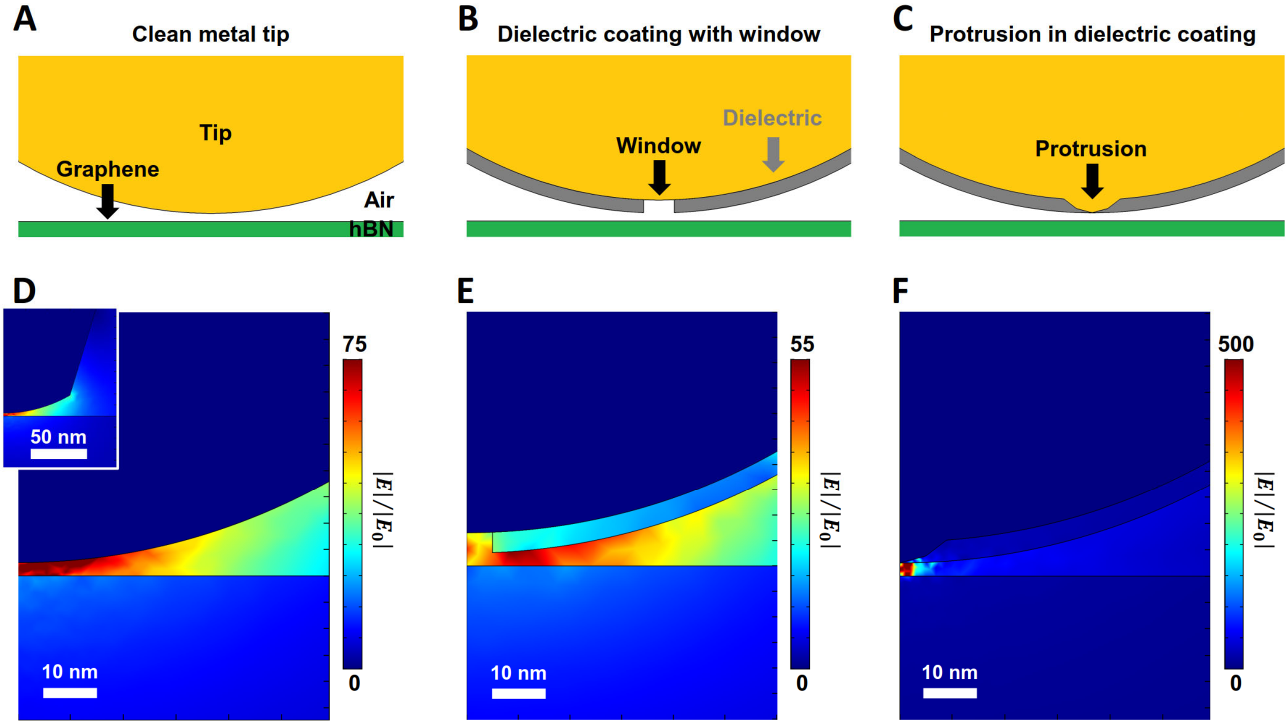

Fig. S15. Electric field enhancement on different tip geometries. (A) The sMIM tip with the unmodified geometry as determined from SEM. **(B)** A hypothetical geometry of an sMIM tip with a uniform coating of dielectrics from sample contaminants, except with a very small window at the tip apex. **(C)** The geometry of tip that we inferred to provide the substantial improvement in the spatial resolution of our uMIM imaging. We consider a metallic tip protrusion in the window opening of the dielectric coating. We hypothesize that similar geometry might be formed after the pre-data collection scanning and cleaning of the sample surface. **(D-F)** The electric field enhancement effect around the tip apex for each geometry shown in figs. S15A-C, respectively. The color scale describes the ratio of the local electric field strength around the tip ($|E_0|$) to the incoming field strength ($|E_0|$). Only one-half of the tip is shown due to the 2D axisymmetry of the geometry. *Inset* in (D): A zoomed-out image of the unmodified tip. This simulation suggests that with the unmodified geometry of the tip (figs. S15A and D) or even with a coated tip without any conducting protrusion (figs. S15B and E), the spatial resolution should still be comparable to the tip diameter, preventing the ultra-high-resolution imaging that can resolve the moiré lattices and isolated moiré defects. Meanwhile, with the tip geometry consisting of the conducting protrusion through the dielectric coating as exemplified in figs. S15C and F, the field enhancement can be strongly localized to within sub-10 nm.

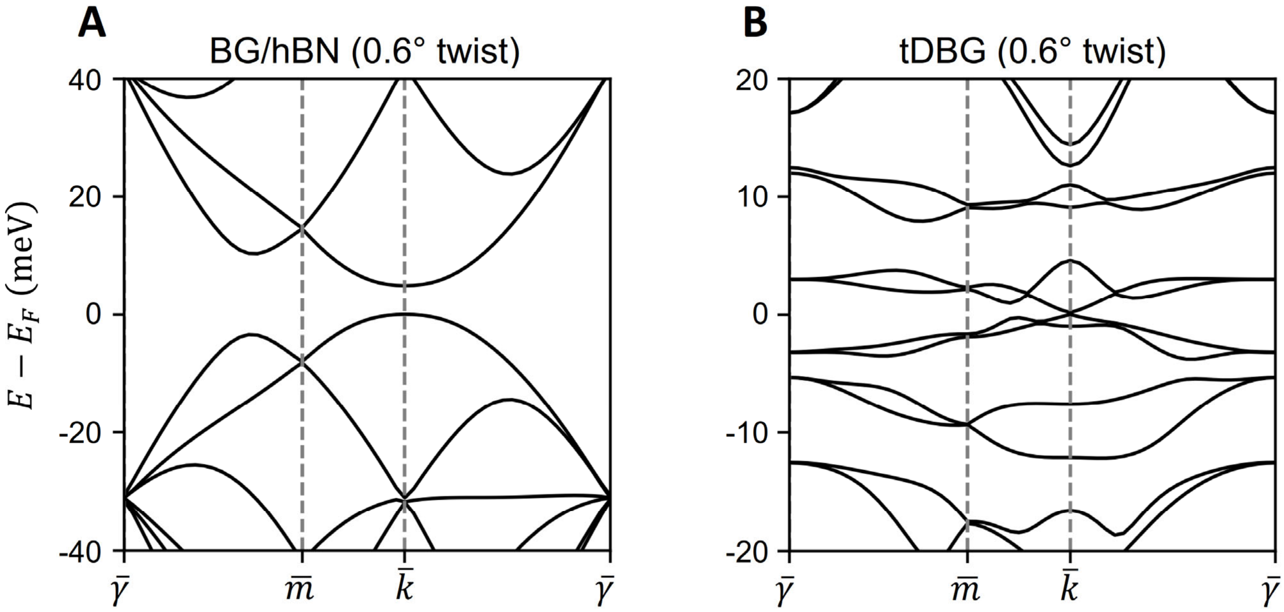

Fig. S16. Calculated band structure of BG/hBN and BG/BG each with ~0.6° twist angle. (A) BG/hBN only. **(B)** tDBG only (*i.e.*, BG/BG) without hBN substrate.